

# The Radial Velocity and Mass of the White Dwarf of EX Hydrae Measured with *Chandra*

*R. Hoogerwerf, N. S. Brickhouse, and C. W. Mauche*

This article to appear in The Astrophysical Journal

**March 4, 2004**

**U.S. Department of Energy**

Lawrence  
Livermore  
National  
Laboratory

## **DISCLAIMER**

This document was prepared as an account of work sponsored by an agency of the United States Government. Neither the United States Government nor the University of California nor any of their employees, makes any warranty, express or implied, or assumes any legal liability or responsibility for the accuracy, completeness, or usefulness of any information, apparatus, product, or process disclosed, or represents that its use would not infringe privately owned rights. Reference herein to any specific commercial product, process, or service by trade name, trademark, manufacturer, or otherwise, does not necessarily constitute or imply its endorsement, recommendation, or favoring by the United States Government or the University of California. The views and opinions of authors expressed herein do not necessarily state or reflect those of the United States Government or the University of California, and shall not be used for advertising or product endorsement purposes.

This is a preprint of a paper intended for publication in a journal or proceedings. Since changes may be made before publication, this preprint is made available with the understanding that it will not be cited or reproduced without the permission of the author.

## **AUSPICES STATEMENT**

This work was performed under the auspices of the U.S. Department of Energy by University of California, Lawrence Livermore National Laboratory under Contract W-7405-Eng-48.

# The Radial Velocity and Mass of the White Dwarf of EX Hydrae Measured with Chandra

R. Hoogerwerf, N. S. Brickhouse

*Smithsonian Astrophysical Observatory, Harvard-Smithsonian Center for Astrophysics, 60 Garden Street, MS 31, Cambridge, MA 02138*

`rhoogerwerf@cfa.harvard.edu, nbrickhouse@cfa.harvard.edu`

and

C. W. Mauche

*Lawrence Livermore National Laboratory, L-473, 7000 East Avenue, Livermore, CA 94550*

`mauche@cygnus.llnl.gov`

## ABSTRACT

We present the first detection of orbital motion in the cataclysmic variable EX Hydrae based on X-ray data from the *Chandra X-ray Observatory*. The large collecting area of the telescope and the high resolution of the HETG spectrometers allow for an unprecedented velocity accuracy of  $\sim 15 \text{ km s}^{-1}$  in the X-ray wavelength regime. We find an emission line velocity amplitude of  $58.2 \pm 3.7 \text{ km s}^{-1}$  and infer a white dwarf mass of  $0.49 \pm 0.13 M_{\odot}$ , in good agreement with previous studies using optical, ultraviolet, and far ultraviolet data.

*Subject headings:* novae, cataclysmic variables—stars: individual (EX Hydrae)—techniques: spectroscopic—x-rays: stars

## 1. Introduction

Magnetic cataclysmic variables (CVs) are semi-detached, interacting binaries consisting of a late-type star that overflows its Roche-lobe and a white dwarf with a magnetic field sufficiently strong to influence the accretion of matter originating from the late-type companion. The magnetic field directs the accretion flow away from the orbital plane and onto both of the white dwarf’s magnetic poles. Accretion behaves differently in the two classes of magnetic cataclysmic variables. In polars the stars are tidally locked; this “static” orientation results

in an accreting flow from the Lagrangian point L1 of the binary along the magnetic field lines of the white dwarf onto its magnetic pole(s). In intermediate polars (IPs), where the white dwarf is spinning faster than the orbital period, matter also accretes onto the white dwarf along the magnetic field lines; however, the matter first accumulates in an accretion disk surrounding the white dwarf. In both polars and IPs the accreting matter approaches the poles of the white dwarf supersonically and so passes through a stand-off shock before cooling and settling onto the white dwarf (Aizu 1973; Kylafis & Lamb 1982).

The cataclysmic variable EX Hydrae belongs to the IP class. It consists of a white dwarf with a spin period of 67 minutes and has an orbital period of 98 minutes. Both the spin period and binary period can be identified in its light curves, from optical (e.g., Vogt, Krzeminski, & Sterken 1980; Sterken et al. 1983), UV (e.g., Mauche 1999; Belle et al. 2003), and X-ray emission (e.g., Watson, Sherrington, & Jameson 1978; Allan, Hellier, & Beardmore 1998). Furthermore, the inclination of the EX Hya system is such that its light curve shows a partial eclipse of the lower accretion pole of the white dwarf by the companion (Allan et al. 1998).

Optical and UV spectroscopy of the EX Hya system has detected the orbital motion associated with the white dwarf (e.g., Breysacher & Vogt 1980; Hellier et al. 1987; Mauche 1999; Belle et al. 2003). This motion, combined with the orbital velocity of the companion and the presence of the eclipse, allows for a mass determination of the white dwarf independent of models of the accretion column. In this letter we use *Chandra* High-Energy Transmission Grating (HETG) data for EX Hya and show that its orbital motion can be detected with high resolution X-ray spectra.

## 2. Observation and Reduction

EX Hya was observed by *Chandra* using the HETG in combination with the Advanced CCD Imaging Spectrometer in its spectroscopy layout (ACIS-S) on 2000 May 18 for 60 ks. The observation was continuous and covers  $\sim 10$  orbital revolutions of the binary system and  $\sim 15$  white dwarf revolutions.

We reduced the data using the *Chandra* Interactive Analysis of Observations (CIAO) software package<sup>1</sup> making only two departures from the standard reduction: 1) we turned randomization off (i.e., we set `rand_pix_size` = 0.0 in the `tg_resolve_events` tool) to minimize any artificial line broadening, and 2) we applied a solar system barycentric correction

---

<sup>1</sup><http://cxc.harvard.edu/ciao/>

so that the event times are in Barycentric Dynamical Time instead of spacecraft time. The reduced HETG EX Hya spectrum, as shown in Figure 1 (see also Mauche 2002; Mukai et al. 2003), reveals emission lines from H- and He-like ions, as well as from Fe L-shell ions, superimposed on a weak continuum. Fe XVII and Fe XXII density diagnostics reported by Mauche, Liedahl, & Fournier (2001, 2003) indicate densities of order  $n_e \approx 10^{14} \text{ cm}^{-3}$ .

### 3. Velocity signature

To search for velocity signatures in the EX Hya HETG data we used the following procedure: 1) identify the spectral lines in the first-order High Energy Grating (HEG) and Medium Energy Grating (MEG) spectra; 2) divide the observation into time segments; 3) add the spectral lines in each time segment to form a composite line profile (CLP) for each grating arm in order to boost the signal-to-noise ratio; 4) measure the line centroid of the CLP; and 5) look for variations of the line centroid with orbital or white dwarf spin phase.

#### 3.1. Line Identification and Wavelength Calibration

Table 1 lists the isolated spectral lines, i.e., lines that do not have another strong line within two times the instrumental FWHM, with a signal-to-noise ratio larger than 10. We obtained the reference wavelengths for these lines from the Astrophysical Plasma Emission Database (APED; Smith et al. 2001). Reference wavelengths with uncertainty estimates from APED are taken from quantum electrodynamic theory for H-like ions (Ericsson 1977) and He-like ions (Drake 1988) and from laboratory measurements for Fe L-shell lines (Brown et al. 1998, 2002). Wavelength uncertainties are for individual lines only and do not include the effects of dielectronic satellite lines that are associated with many of these strong lines. Such blending satellite lines contribute less than a few percent to the strength of the emission feature.

We defined unblended lines as either single lines or multiplets that are unresolved and from the same ion. For unresolved lines from the same ion we used the emissivity-weighted wavelengths. The He-like Mg and Si forbidden and intercombination lines are unresolved by MEG, and since their theoretical line flux ratios depend on electron density and photoexciting radiation, we cannot weight their wavelengths by the low-density emissivities tabulated in APED. Thus we excluded these lines from the CLP.

To confidently add spectral lines it is important to verify the wavelength calibration and to correct for any systematic offsets between the observed line centroids and the reference

wavelengths from the APED database. To fit the emission lines we first determined the contribution of the continuum emission to the spectrum. A global fit to line-free regions of HEG and MEG spectra using the Astrophysical Plasma Emission Code model, (APEC, version 1.3, Smith et al. 2001) allows a self-consistent treatment of the continuum for all lines. We defined the line-free regions as any part of the spectrum greater than 0.1 Å in width that is devoid of spectral lines with emissivities larger than  $10^{-18}$  ph cm<sup>3</sup> s<sup>-1</sup> (this is  $\sim 1/1000$  of brightest line in the spectrum) in the APED database. We found a good fit for a thermal continuum (consisting of bremsstrahlung, radiative recombination, and two-photon emission) for a temperature of  $16 \pm 1$  keV (see Figure 1), in good agreement with the shock temperature of  $15.4^{+5.3}_{-2.6}$  keV reported by Fujimoto & Ishida (1997) for an Aizu (1973) model fitted to the *ASCA* spectrum of EX Hya, and the maximum temperature of 20 keV reported by Mukai et al. (2003) for a cooling flow model fitted to the same *Chandra* HETG data. A two-temperature continuum model did not significantly lower the  $\chi^2$  of the fit. This is not surprising since the highest temperatures dominate the emission measure distribution in an accretion column cooling mainly by means of thermal bremsstrahlung.

To determine if any offsets between the observed wavelengths and their reference values exist we performed the following fit. We set the distances between each consecutive pair of emission lines equal to their separation based on the APED database and only fit the normalization of each line and the overall wavelength offset. Each line is modeled using a Gaussian with a FWHM equal to the instrumental FWHM (0.012 Å for HEG and 0.023 Å for MEG). This resulted in the following offsets for each of the orders (predicted – observed wavelength):  $-0.0012(2)$ ,  $-0.0020(2)$ ,  $-0.0008(2)$ , and  $0.0004(2)$  Å for HEG–1, HEG+1, MEG–1, and MEG+1, respectively. Although the offsets are small, they do constitute  $\sim 10\%$  of the HEG FWHM and  $\sim 5\%$  of the MEG FWHM, or about 30–50 km s<sup>-1</sup> (at 10 Å), and need to be corrected for.

Even more important than the absolute and relative wavelength calibration is its stability during an observation; this appears to be extremely stable (*Chandra* Proposers Observatory Guide<sup>2</sup>). Furthermore, the rotation and orbital periods of the EX Hya system are not relevant timescales for the satellite (dither period is 707.1 sec in the pitch direction and 1000 sec in the yaw direction).

---

<sup>2</sup><http://cxc.harvard.edu/proposer/POG/index.html>

### 3.2. Binary

To look for changing velocities associated with the binary period in the *Chandra* HETG data for EX Hya we first phase folded the spectra (using the ephemeris of Hellier & Sproats 1992) and divided the observation into phase intervals centered at  $\phi_{98} = 0.05, 0.10, \dots, 0.95, 1.00$ . with a width of  $\Delta_{\phi_{98}} = 0.25$ , where  $\phi_{98}$  indicates the phase in the binary orbit. Note that the phase intervals are overlapping.

Unfortunately, by splitting the observation into smaller phase intervals none of the spectral lines have sufficient signal-to-noise ratio to confidently measure changes in their wavelengths. We therefore added all lines in each interval to accumulate enough counts to accurately measure the central wavelength. We accomplished this by the following procedure: 1) For each grating first-order arm we determined the count-weighted average wavelength of the lines in Table 1,  $\bar{\lambda} = \sum_i c_i \lambda_{\text{ref},i} / \sum_i c_i$ , where  $c_i$  is the number of counts in the spectrum for a segment  $2 \times \text{FWHM}$  wide centered on  $\lambda_{\text{ref},i}$  (from Table 1) minus the number of counts predicted by the model continuum (see §3.1). 2) Each line in the spectrum was shifted by an amount equal to its reference wavelength,  $\lambda_{\text{ref},i}$  and by the wavelength calibration correction (see §3.1). 3) The wavelength-binned shifted spectrum was then transformed to a velocity-binned spectrum according to  $v_{\text{bin},i} = c(\lambda_{\text{bin},i} - \lambda_{\text{ref},i}) / \lambda_{\text{ref},i}$ . 4) The shifted velocity-binned profile for each spectral line was added to form one line profile. However, since the bin size for each line was different we chose to rebin each  $v_{\text{bin},i}$  to the bin size corresponding to  $\bar{\lambda}$ :  $\bar{v}_{\text{bin}} = c(\lambda_{\text{bin}} - \bar{\lambda}) / \bar{\lambda}$ . 5) Finally, we measured the central velocity for this composite line profile (CLP).

Figure 2 shows the CLPs for binary phases  $\phi_{98} = 0.00, 0.25, 0.50$ , and  $0.75$ . The change in CLP centroid is clearly visible showing how powerful the combination of a large effective area and high spectral resolution can be in the X-ray regime.

The radial velocity shifts as a function of  $\phi_{98}$  for the combined orders MEG–1 plus MEG+1 are shown in the top panel of Figure 3. We present the MEG data rather than the HEG data because they have a factor of 2–10 times more counts per spectral line, which improves our centroiding accuracy even with the lower resolution of the MEG instrument (see also §5). Results from the HEG and the individual MEG orders are consistent but with lower significance. The figure clearly shows that there is a systematic motion of the CLP with a period equal to that of the binary. The solid line represents the following fit to the data points:

$$v(\phi) = \frac{1}{\Delta} \int_{\phi-\Delta/2}^{\phi+\Delta/2} \gamma + K \sin \left( 2\pi \frac{(\tilde{\phi} - \phi_0)}{\omega} \right) d\tilde{\phi}, \quad (1)$$

where  $\gamma = 1.3 \pm 2.3 \text{ km s}^{-1}$ ,  $K = 58.2 \pm 3.7 \text{ km s}^{-1}$  is the velocity amplitude,  $\phi_0 = 0.48 \pm 0.01$ ,  $\omega$  is fixed to 1.0, and  $\Delta = 0.25$ . Since the data points overlap, and are thus correlated, we calculated  $\chi^2$  for each of the five sets of independent data points (indicated in Figure 3). The  $\chi^2$  per degree of freedom (dof) for the independent data sets range from  $\chi^2/(\text{dof} = 1) = 0.1$  to 1.0. It is important to note that the value of  $\chi^2$  for a small number of dof can be different from the value one expects to indicate a good fit in the case of a large number of dof, i.e.,  $\chi^2/\text{dof} = 1.0$ . The important statistic is  $Q(\chi^2|\text{dof})$ , which is the probability that the observed chi-squared will exceed the value  $\chi^2$ . Acceptable values for  $Q$ , i.e., the  $3\sigma$  confidence interval, range from  $\sim 0.0015$  to  $\sim 0.9985$ . For the above values of  $\chi^2/\text{dof}$ ,  $Q$  ranges from 0.3 to 0.8.

We also fitted the data with 1) a constant velocity and 2) a sine curve with the period not forced to the binary phase, i.e.,  $\omega$  not fixed to 1.0 in Eq. 1. The former fit yields  $\gamma = -2.8 \pm 2.3 \text{ km s}^{-1}$ ,  $\chi^2/(\text{dof} = 3)$  ranges from 13 to 19, and  $Q \approx 7.0 \times 10^{-11}$ , while the latter fit yields a period of  $\omega = 1.01 \pm 0.04$  times the binary period, and values of  $\gamma$ ,  $K$ , and  $\phi_0$  are indistinguishable from the fit described above. The latter fit has zero degrees of freedom and hence a meaningless  $\chi^2$ .

The above velocity amplitude and phase offset,  $K = 58.2 \pm 3.7 \text{ km s}^{-1}$ , and  $\phi_0 = 0.48 \pm 0.01$  are in good agreement with those reported by Breysacher & Vogt (1980,  $K = 68 \pm 9 \text{ km s}^{-1}$ ,  $\phi_0 = 0.5$ ), Cowley, Hutchings, & Crampton (1981,  $K = 90 \pm 28 \text{ km s}^{-1}$ ,  $\phi_0 = 0.55$ ), Gilliland (1982,  $K = 58 \pm 9.3 \text{ km s}^{-1}$ ,  $\phi_0 = 0.52$ ), Hellier et al. (1987,  $K = 69 \pm 9 \text{ km s}^{-1}$ ,  $\phi_0 = 0.53 \pm 0.03$ ), Mauche (1999,  $K = 85 \pm 9 \text{ km s}^{-1}$ ,  $\phi_0 = 0.54 \pm 0.02$ , using FUV lines), and Belle et al. (2003,  $K = 59.6 \pm 2.6 \text{ km s}^{-1}$ ,  $\phi_0 = 0.48 \pm 0.05$ , using UV lines).

### 3.3. White Dwarf Spin

The bottom panel of Figure 3 shows the CLP radial velocity versus the white dwarf spin period using bins of size one-third the spin period (i.e.,  $\Delta = 0.333$ ). The velocities have been corrected for the average binary motion for each data point based on the fit described in §3.2. To provide upper limits on the rotation velocity of the white dwarf and the infall velocities in the accretion column, we fitted sine curves to these data. We assumed that the upper accretion column is pointing away from the observer at white dwarf phase 0 (consistent with both the accretion curtain model Rosen et al. 1988 and the accretion pole occultation model Allan et al. 1998) and that the cooler part of the lower accretion column, where most of the spectral lines are formed, is not visible throughout most of the spin cycle (Allan et al. 1998). The dotted curve in the figure represents the best-fit rotation velocity of  $9.2 \pm 5.0 \text{ km s}^{-1}$  ( $\phi_0 = 0.50$ ) and the dashed curve represents the best-fit infall velocity of  $7.9 \pm 5.4 \text{ km s}^{-1}$ .



( $\phi_0 = 0.25$ ). The  $3\sigma$  upper limits on the rotation and infall velocities are thus  $\sim 25 \text{ km s}^{-1}$ .

#### 4. White Dwarf Mass

Combining the orbital motion of the white dwarf obtained in §3.2 with the orbital motion of the companion (Vande Putte et al. 2003,  $K_2 = 360 \pm 35 \text{ km s}^{-1}$ ) and the eclipse duration (Mukai et al. 1998) allows us to determine the white dwarf mass  $M_1$ , companion mass  $M_2$ , and inclination  $i$  of the EX Hya system.

Here we followed the approach taken by Beuermann et al. (2003) using a computer program kindly provided to us by K. Beuermann. Assuming that the emission originates at or near the pole of the white dwarf, the iterative method yields  $M_1 = 0.49 \pm 0.13 M_\odot$ ,  $M_2 = 0.078 \pm 0.014 M_\odot$ ,  $i = 77.2 \pm 0.6^\circ$ . The white dwarf mass  $M_1$  corresponds to a white dwarf radius  $R_1 = 1.0 \pm 0.2 \times 10^9 \text{ cm}$  (Wood 1995). If the emission originates above the surface of the white dwarf the inclination of the system decreases  $\sim 0.1^\circ$  for every  $0.1 \times R_1$  in elevation above the surface. These results agree within the errors with those found by Beuermann et al. (2003) and hence do not change any of the conclusions on the accretion rate reached in that paper.

Finally, we note that our estimate of the white dwarf mass, which is based on the radial velocity of the emission lines in the *Chandra* HETG spectrum, agrees with that of Fujimoto & Ishida (1997) ( $M_1 = 0.48^{+0.10}_{-0.06} M_\odot$ ), which is based on the H- to He-like emission line intensity ratios observed in the *ASCA* spectrum. Our “classical” radial velocity result is applicable only to high-inclination magnetic CV binaries, whereas theirs is applicable to a wide range of polars and IPs, although it relies on theoretical models of accretion column.

#### 5. Discussion

Our radial velocity measurement in EX Hya pushes the instrumental limit of the *Chandra* grating instruments. The MEG instrument has an effective area large enough to accumulate between 3000 and 4000 counts in the CLP so that we can reliably find the centroid to an accuracy of  $\sim 0.5 \text{ mÅ}$ , corresponding to an accuracy in velocity space of  $10\text{--}15 \text{ km s}^{-1}$  (at  $\sim 10 \text{ Å}$ ). This is consistent with the statistical uncertainty for measuring Gaussian line centroids derived by Landman, Roussel-Dupré, & Tanigawa (1982):

$$S_\mu = \sigma \left( \frac{2}{\pi} \right)^{1/4} (\Delta x)_0^{1/2} \bar{\Delta}, \quad (2)$$

where  $S_\mu$  is the statistical uncertainty in  $\mu$  (the line center),  $\sigma$  is the instrumental resolution (FWHM/2.3548),  $(\Delta x)_0$  is the bin size expressed in terms of  $\sigma$ , and  $\bar{\Delta}$  is the average error expressed in terms of the peak amplitude. For our MEG CLP this equation yields 0.5 mÅ, as observed, where we have taken  $\bar{\Delta} = 2/\sqrt{P}$ , with  $P$  the number of counts in the peak bin of the CLP.

Unfortunately the effective area of the HEG instrument is significantly smaller (a factor of 3 at 10 Å) and does not allow us to improve over the MEG despite the better instrumental resolution ( $S_\mu = 0.5$  mÅ for HEG, similar to MEG). This means that for this EX Hya data set we obtain similar velocity accuracies for HEG and MEG. To fully exploit the HEG resolution, i.e., gain a factor of 2 in velocity accuracy, a significantly longer observation would be required.

More velocity resolution is desirable to detect velocity changes induced by the rotation of the white dwarf around its spin axis. Such velocity signatures would provide information on the location and velocity of the emitting plasma and on the location of the magnetic pole. The lack of a pronounced velocity variation at the spin period of the white dwarf in this HETG observation is expected. To see this, note that the free-fall velocity onto the white dwarf  $v_{\text{ff}} = (2GM_1/R_1)^{1/2} \approx 3600 \text{ km s}^{-1}$ , and the immediate post-shock velocity  $v = v_{\text{ff}}/4 \approx 900 \text{ km s}^{-1}$ . Also note that the majority of the spectral lines in the HETG spectrum are formed at temperatures of less than 2 keV, i.e., 0.1 times the post-shock temperature  $T = 3GM_1 m_{\text{H}} \mu / 8kR_1 \approx 20 \text{ keV}$  ( $\mu = 0.615$  is the mean molecular weight of a completely ionized plasma of solar composition). From Figures 1 and 2 of Aizu (1973) we estimate the velocity of the 2 keV gas to be  $0.1 v \approx 90 \text{ km s}^{-1}$ . Assuming that the accretion columns are perpendicular to the orbital plane, the projected post-shock velocity  $v \cos i \approx 18 \text{ km s}^{-1}$ . Furthermore, the maximum rotational velocity of the white dwarf  $v_{\text{rot}} = 2\pi R_1 / 67 \text{ min} \approx 15 \text{ km s}^{-1}$ . Both velocities are smaller than the upper limits derived in §3.3.

## 6. Conclusions

We have confirmed the orbital velocity of the white dwarf in the cataclysmic variable EX Hya using the *Chandra* HETG. This measurement is the first detection of orbital motion in a CV binary system based on X-ray spectroscopy. By adding various spectral lines visible in the EX Hya spectrum enough signal-to-noise can be accumulated to obtain velocities accurate to 10–15 km s<sup>−1</sup>. No new conclusions are drawn on the white dwarf mass ( $0.49 \pm 0.13 M_\odot$ ).

We thank Klaus Beuermann for his assistance in determining the white dwarf mass. We thank H. Tananbaum for the generous grant of Director’s Discretionary Time that made possible the *Chandra* observations of EX Hya. Support for this work was provided in part by NASA through *Chandra* Award Number DD0-1004B issued by the *Chandra* X-Ray Observatory Center, which is operated by the Smithsonian Astrophysical Observatory for and on behalf of NASA under contract NAS8-39073. We acknowledge support from NASA LTSA NAG5-3559 and Chandra grant GO2-3018x. NSB was supported by NASA contract NAS8-39083 to the Smithsonian Astrophysical Observatory (SAO) for the Chandra X-Ray Center (CXC). CWM’s contribution to this work was performed under the auspices of the US Department of Energy by University of California Lawrence Livermore National Laboratory under contract W-7405-Eng-48.

## REFERENCES

- Aizu, K. 1973, Prg. Theor. Phys., 49, 1184
- Allan, A., Hellier, C. H., & Beardmore, A. 1998, MNRAS, 295, 167
- Belle, K. E., Howell, S. B., Sion, E. M., Long, K. S., & Szkody, P. 2003, ApJ, 587, 373
- Beuermann, K., Harrison, Th. E., McArthur, B. E., Benedict, G. F., & Gänsicke, B. T. 2003, A&A, 412, 821
- Breysacher, J., & Vogt, N. 1980, A&A, 87, 349
- Brown, G. V., Beiersdorfer, P., Liedahl, D. A., Widmann, K., & Kahn, S. M. 1998, ApJ, 502, 1015
- Brown, G. V., Beiersdorfer, P., Liedahl, D. A., Widmann, K., Kahn, S. M., & Clothiaux, E. J. 2002, ApJS, 140, 589
- Cowley, A. P., Hutchings, J. B., & Crampton, D. 1981, ApJ, 246, 489
- Drake, G. W. 1988, Can. J. Phys. 66, 586
- Ericsson, G. W. 1977, J. Phys. Chem. Ref. Data, 6, 3
- Fujimoto, R., & Ishida, M. 1997, ApJ, 474, 774
- Gilliland, R. L. 1982, ApJ, 258, 576
- Hellier, C., Mason, K. O., Rosen, S. R., & Córdova, F. A. 1987, MNRAS, 228, 463

- Hellier, C., & Sproats, L. N. 1992, *IBVS*, 3724, 1
- Kylafis, N. D., & Lamb, D. Q. 1982, *ApJS*, 48, 239
- Landman, D. A., Roussel-Dupré, R., & Tanigawa, G. 1982, *ApJ*, 261, 732
- Mauche, C. W. 1999, *ApJ*, 520, 822
- Mauche, C. W. 2002, *ASP Conf. Ser.* 261: The Physics of Cataclysmic Variables and Related Objects, eds. B. T. Gänsicke, K. Beuermann, and K. Reinsch (San Francisco: ASP), 113
- Mauche, C. W., Liedahl, D. A., & Fournier, K. B. 2001, *ApJ*, 560, 992
- Mauche, C. W., Liedahl, D. A., & Fournier, K. B. 2003, *ApJ*, 588, L101
- Mukai, K., Ishida, M., Osborne, J., Rosen, S., & Stavroyiannopoulos, D. 1998, *ASP Conf. Ser.* 137: Wild Stars in the Old West, eds. S. Howell, E. Kuulkers, and C. Woodward (San Francisco: ASP), 554
- Mukai, K., Kinkhabwala, A., Peterson, J. R., Kahn, S. M., & Paerels, F. 2003, *ApJ*, 586, L77
- Rosen, S. R., Mason, H. O., & Córdoba, F. A. 1988, *MNRAS*, 231, 549
- Smith, R. K., Brickhouse, N. S., Liedahl, D. A., & Raymond, J. C. 2001, *ApJ*, 556, L91
- Sterken, C., Vogt, N., Freeth, R., Kennedy, H. D., Marino, B. F., Page, A. A., & Walker, W. S. G. 1983, *A&A*, 118, 325
- Vande Putte, D., Smith, R. C., Hawkins, N. A., & Martin, J. S. 2003, *MNRAS*, 342, 151
- Vogt, N., Krzeminski, W., & Sterken, C. 1980, *A&A*, 85, 106
- Watson, M. G., Sherrington, M. R., & Jameson, R. F. 1978, *MNRAS*, 184, 79
- Wood, M. A., 1995, in *Lecture Notes on Physics*, eds. D. Koester, and K. Werner, *LNP*, 443, 41

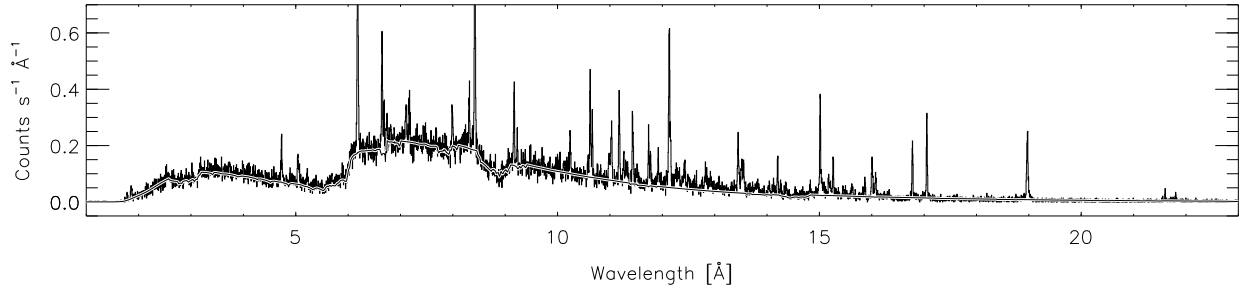


Fig. 1.— Spectrum for the combined first orders of the MEG instrument. Smooth curve represents the one-temperature thermal continuum model fit to the spectrum.

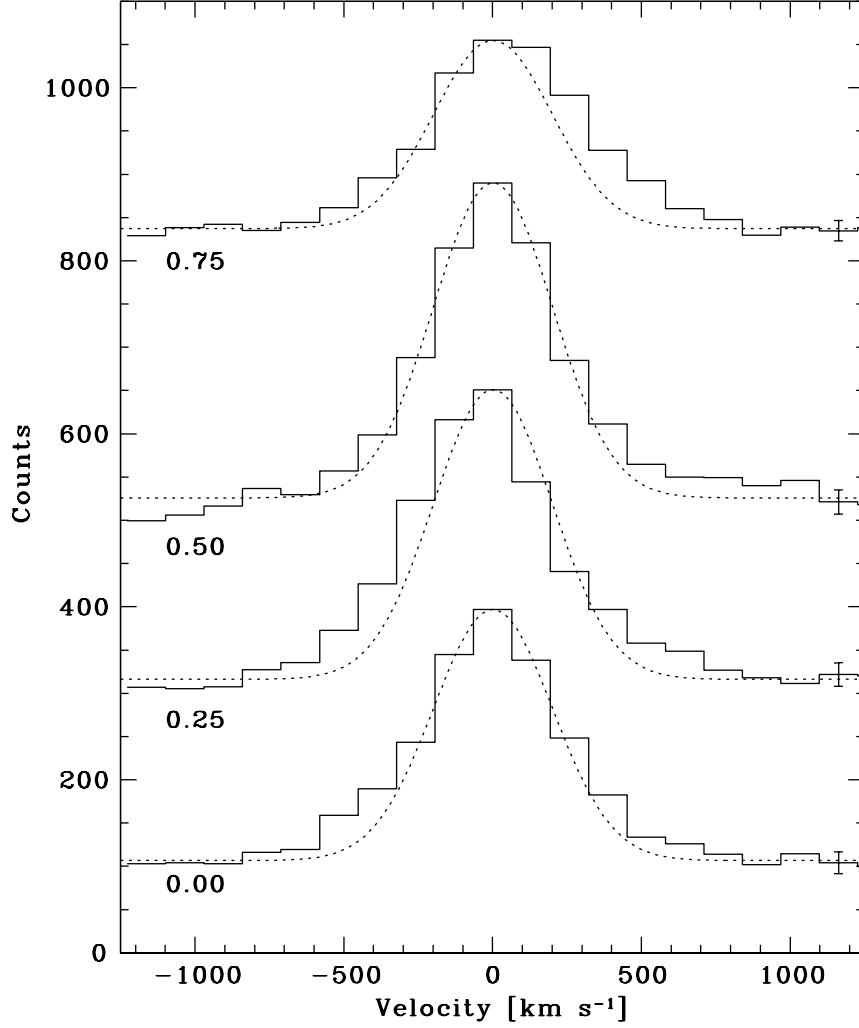


Fig. 2.— Composite line profiles (CLPs) based on the first-order MEG data for the non-blended lines of EX Hya for binary phases 0.00, 0.25, 0.50, and 0.75 (shifted in the vertical direction by 200, 400, and 720 counts, respectively, to separate the profiles). The average error on the CLP bins is depicted in the last bin of each CLP. Dotted line profiles represent the instrumental profile of the CLP (normalized at the peak) at a constant velocity of  $1.3 \text{ km s}^{-1}$ . Number of counts in the 0.75 profile is lower because this binary phase corresponds to the bulge absorption feature in the EX Hya light curve.

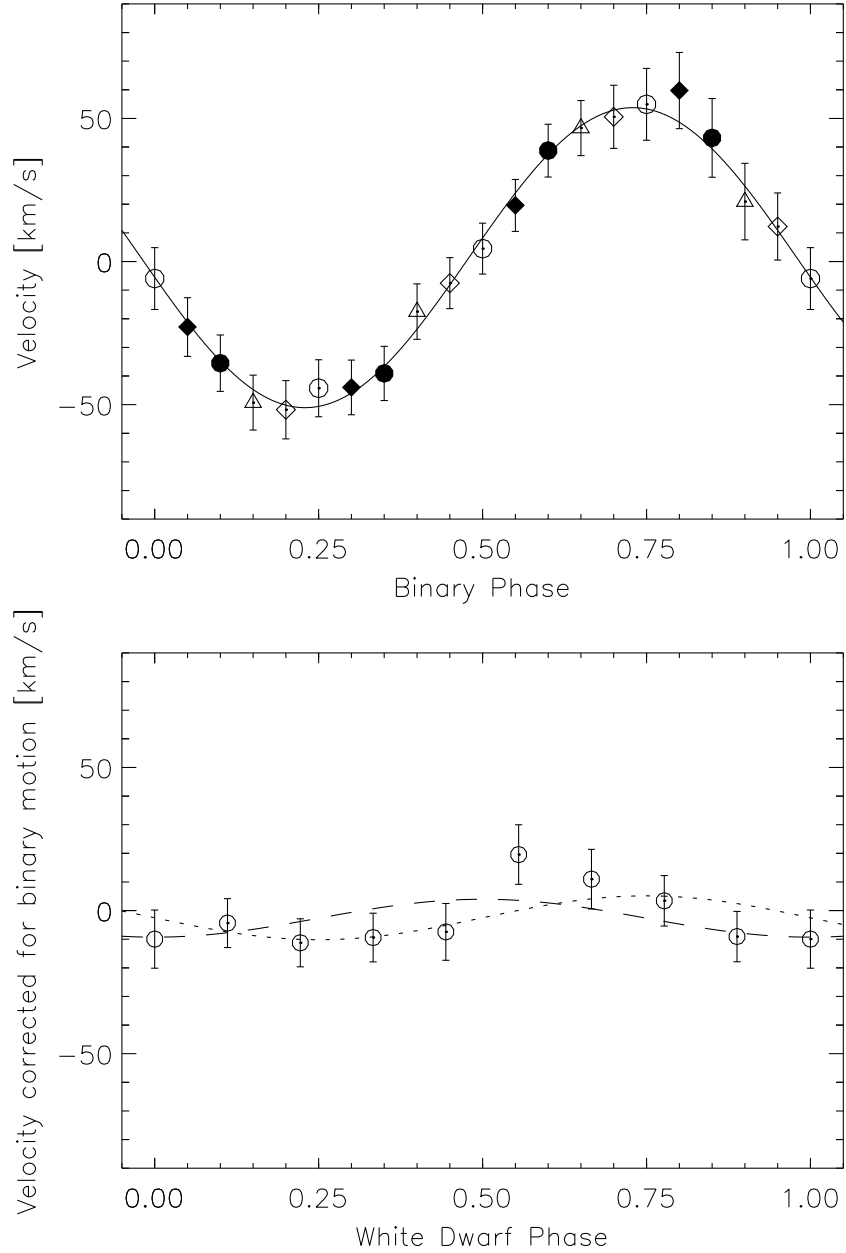


Fig. 3.— Top panel: CLP radial velocity versus the binary period based on the first-order MEG data. Solid curve represents the sinusoidal fit to the data. The five sets of independent points have been indicated by different symbols (see §3.2). Bottom panel: CLP radial velocity (corrected for the binary motion) versus the white dwarf spin period. Dotted curve represents the best-fit velocity curve corresponding to the rotation velocity of the white dwarf and the dashed line represents the best-fit velocity curve corresponding to the infall velocity in the accretion column (see §3.3).

Table 1. Strong EX Hydrae HETG spectral lines

Ion	Upper level	Lower level	Wavelength <sup>a</sup> [Å]
Fe XXVI	$2p^2 P_{1/2,3/2}$	$1s^2 S_{1/2}$	1.780
S XVI	$2p^2 P_{1/2,3/2}$	$1s^2 S_{1/2}$	4.729
S XV	$1s2p^1 P_1$	$1s^2^1 S_0$	5.039
Si XIV	$2p^2 P_{1/2,3/2}$	$1s^2 S_{1/2}$	6.182
Si XIII	$1s2p^1 P_1$	$1s^2^1 S_0$	6.648
Si XIII <sup>b</sup>	$1s2p^3 P_{1,2}$	$1s^2^1 S_0$	6.687
Fe XXIV	$4p^2 P_{1/2,3/2}$	$2s^2 S_{1/2}$	7.989
Mg XII	$2p^2 P_{1/2,3/2}$	$1s^2 S_{1/2}$	8.421
Mg XI	$1s2p^1 P_1$	$1s^2^1 S_0$	9.169
Mg XI <sup>b</sup>	$1s2p^3 P_{1,2}$	$1s^2^1 S_0$	9.231
Ne X	$3p^2 P_{1/2,3/2}$	$1s^2 S_{1/2}$	10.239
Fe XXIV	$3d^2 D_{5/2}$	$2s^2 S_{1/2}$	11.176
Fe XXIV <sup>c</sup>	$3s^2 S_{1/2}$	$2p^2 P_{3/2}$	11.432
Fe XXIII	$2s3d^1 D_2$	$2s2p^1 P_1$	11.736
Ne X <sup>d</sup>	$2p^2 P_{1/2,3/2}$	$1s^2 S_{1/2}$	12.132
Ne IX	$1s2p^1 P_1$	$1s^2^1 S_0$	13.447
Fe XVIII	$2p_{1/2}2p_{3/2}^3 3d_{5/2}$	$2p^5^2 P_{3/2}$	14.208
	$2p^4(^1 D)3d^2 D_{5/2}$	$2p^5^2 P_{3/2}$	
Fe XVII	$2p^5(^2 P)3d^1 P_1$	$2p^6^1 S_0$	15.014
Fe XVII	$2p^5(^2 P)3d^3 D_1$	$2p^6^1 S_0$	15.261
Fe XVIII <sup>e</sup>	$2p^4(^3 P)3s^2 P_{3/2}$	$2p^5^2 P_{3/2}$	16.005
Fe XVII	$2p^5(^2 P)3s^1 P_1$	$2p^6^1 S_0$	16.780
Fe XVII	$2p^5(^2 P)3s^3 P_1$	$2p^6^1 S_0$	17.051
O VIII	$2p^2 P_{1/2,3/2}$	$1s^2 S_{1/2}$	18.968

<sup>a</sup>All wavelength errors are better and 0.004 Å.

<sup>b</sup>The unresolved He-like forbidden and intercombination lines for Si and Mg are not considered in the velocity analysis.

<sup>c</sup>Blend consists of the Fe XXIV, Fe XVIII  $2p^4(^3 P)4d^2 F_{5/2}$  to  $2p^5^2 P_{3/2}$ , and Fe XXII  $2s2p_{1/2}3p_{3/2}$  to  $2s^2 2p^2 P_{1/2}$  lines. We adopted the wavelength for Fe XXIV since most flux seems to be contained in this line.

<sup>d</sup>Blend consists of the Ne X Ly  $\alpha$  doublet, Fe XVII  $2p^5(^2 P)4d^1 P_1$  to  $2p^6^1 S_0$ , and Fe XXII  $2p(^3 P)3d^4 D_{5/2}$  to  $2p^2^2 D_{5/2}$  lines.

<sup>e</sup>Blend consists of the Fe XVIII and O VIII  $3p^2 P_{1/2,3/2}$  to  $1s^2 S_{1/2}$  lines.



---

---

---

---

---

---